Aerosol Science and Technology ›
Volume 39, 2005 - Issue 12

Free access

Listen

Miscellany

Design, Modeling, Optimization, and Experimental Tests of a Particle Beam Width Probe for the Aerodyne Aerosol Mass Spectrometer

J. Alex Huffman, John T. Jayne, Frank Drewnick, Allison C. Aiken, Timothy Onasch, Douglas R. Worsnop & ...show all

Pages 1143-1163 | Received 10 Apr 2005, Accepted 19 Oct 2005, Published online: 23 Feb 2007

Cite this article https://doi.org/10.1080/02786820500423782

Aerodyn allowing the introduc sequent analysis ynamic lens is of inte easured particle spherical partic stant lens press or these reasons, or the Aerodyn applicable to other ted here consists lock the

beam. A computer model was developed to optimize the BWP and interpret its experimental data. Model assumptions were found to be reasonably accurate for all laboratory-generated particle types to which the model was compared. Comparisons of particle beam width data from a number of publications are also shown here. Particle losses due to beam broadening are found to be minor for the AMS for both laboratory and ambient particles. The model was then used to optimize the choice of the BWP dimensions, and to guide its use during continuous operation. A wire diameter approximately 1.55 times larger than the beam width to be measured provides near optimal sensitivity toward both collection efficiency and surrogate non-sphericity information. Wire diameters of 0.62 mm and 0.44 mm (for the AMS “long” and “short” chambers, respectively) provide reasonable sensitivity over the expected range of particle beam widths, for both spherical and non-spherical particles. Three other alternative BWP geometries were also modeled and discussed.

1. INTRODUCTION

The development of aerodynamic lens inlets in the last decade has revolutionized the way particles can be focused into very narrow beams for subsequent analysis. Aerodynamic lenses were first demonstrated by the group of P.H. McMurry at the University of Minnesota (Liu et al. 1995a, 1995b) and have been the subject of a number of characterization and customization studies by several groups (Petrucci et al. 2000; Sc ng et al. 2002; Zh rough which a gas (and particle) s and particle within a given aracteristics of th scussed in more de

As partic tightly focused ut small radial ve wnian

irregular particles result in additional radial velocity components and divergence of the particle trajectories (Liu et al. 1995a). For this reason, beams comprised of spherical particles have the tightest focusing for a given particle size, and broader beams are observed when sampling irregular particles (Jayne et al. 2000; Kane and Johnston 2000; Liu et al. 1995b; Schreiner et al. 1998; Tobias et al. 2000). This beam broadening has two practical implications: (1) the beam solid angle may become so large that a measurable fraction of particles may miss the detection system in some instruments, resulting in a sampling bias correlated with particle shape (and also with composition if shape and composition are related); and (2) the degree of beam broadening with respect to spherical particles of the same size can be used as a real-time surrogate measurement of particle non-sphericity (under constant lens pressure conditions).

Currently, many particle mass spectrometers utilize aerodynamic lenses in order to introduce particles into a vacuum system for real-time analysis (Cziczo et al. 2003; Jayne et al. 2000; Mahadevan et al. 2002; Oktem et al. 2004; Schreiner et al. 2002; Su et al. 2004; Svane et al. 2004; Sykes et al. 2002; Tobias et al. 2000; Zelenyuk et al. 1999). The Aerodyne Aerosol Mass Spectrometer (AMS) has recently been commercialized and it is currently the most commonly used real-time particle mass spectrometer. The AMS can provide real-time information on mass concentrations of chemical species in/on submicron aerosols, as well as on chemically resolved size distributions (Jayne et al. 2000; Jimenez et al. 2003b). Submicron aerosols entering the AMS are focused into a narrow beam via an aerodynamic lens (Zhang et al. 2002, 2004c), and reach a terminal velocity that is a function of their vacuum aerodynamic diameter, d_{va} (DeCarlo et al. 2004; Jimenez et al. 2003a). The AMS measures particle size by c ayne et al. 2000; Jir n-refractory particles flash-vaporize of every million o EI) at 70 eV. In th pole mass analy ion time-of-flight AM quadrupole mass an ck et al. 2004). S) are achieved erent

dimensions of the two AMS chamber designs, and Figure 1 shows a depiction of the chamber geometries and distances. Jayne et al. (2000) and Jimenez et al. (2003b) describe the instrument in more detail.

FIG. 1 Schematic diagram of relative location of vaporizer, and BWP for the two current AMS configurations. Beam widths, σ, are shown in the plane which they reference. See Table 3.

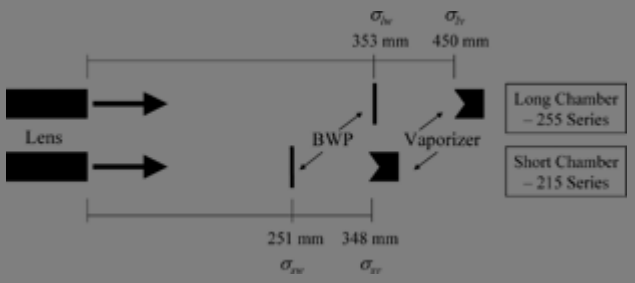

Display full size

TABLE 1 Particle flight distance, vaporizer (or laser spot) size, and solid angles of collection for the detection geometries of the long-chamber and short-chamber AMS, and two laser ablation particle mass spectrometers (Cziczo et al. 2003 ; Gard et al. 1997). The solid angle of detection represents the geometric area sampled by the vaporization laser or vaporizer at the given particle flight distance from the lens exit

Download CSV Display Table

Fluid dyn…S, suggest 100% tra…nm, with reduced …1500 nm, and allow…oximately 10^7 over…z et al. 2003b)…er AMS were…types that had bee… 2000). There is…pes (such as flame so…% of the particles…al. 2004). A

lack of detection for such non-spherical particles would result in a bias in their reported mass and number concentrations.

While the width of the beams produced by most particle types appears to be narrow enough for all particles to impact the AMS vaporizer, it is important to be able to verify this in real-time in the AMS and in other instruments that use aerodynamic lens inlets. Previous measurements of particle beam width were carried out by using a moveable knife-edge (Liu et al. 1995b; Schreiner et al. 1999; Schreiner et al. 1998) or wire (Jayne et al. 2000) to partially block the beam, while measuring the reduction in particle signal; by changing the lens aim, and measuring the resultant change in signal (Jayne et al. Aerodyne Research, unpublished results); qualitatively by measuring loss in total signal with respect to spherical particles (Tobias et al. 2000); and by measuring the hit rate by an ablation laser as it is translated across the particle beam (Kane and Johnston 2000; Su et al. 2004). Of those methods, the intermittent blockage of the particle beam is best suited to the rapid real-time measurement of particle beam width. Thus, in order to enable real-time quantification of surrogate particle non-sphericity and of the shape-related collection efficiency (E_s) of the AMS, a particle-beam width probe (BWP) has been designed and constructed. This paper presents a model of the effect of the particle BWP on particle signal as a function of particle beam and probe widths. The model is based on the assumption that particle density within the beam is described as a 2-D circular Gaussian distribution. This assumption is tested experimentally using monodisperse particles of several pure compositions. The model is then used to optimize the probe design, to study the collection of very irregular particle beams, and to evaluate alternative probe geometries. The results presented here focus on the AMS, but are a ets.

2. ME

2.1.

To chara ine here the AMS coll e size for a given pa rticles physical rodynamic diamete definition

et al. 2002, 2004c). The current understanding of particle detection in the AMS indicates that a fraction of low-volatility solid particles such as $(NH_4)_2SO_4$ can also go undetected due to bounce off the vaporizer surface for the current vaporizer design. This gives rise to another collection efficiency term due to particle bounce, for a given particle composition and phase, $E_b(d_{va})$. The overall mass-based total collection efficiency CE for the AMS was defined previously as the fraction of the particle mass that is detected compared to what would be detected if the particles were spherical and no particles were lost due to bouncing off the vaporizer (Alfarra et al. 2004). It is very important to note that some particle mass may go undetected because of the limited transmission of the AMS inlet and aerodynamic lens for spherical particles at the upper and lower limits of its transmission window. We define here the transmission efficiency of the inlet and lens for spheres as $E_L(d_{va})$. The upper limit of transmission depends on the specific aerodynamic lens being used, but is typically around 1.5 μ m, and the particle mass measurement of the AMS is reported as approximately PM_1. $E_s(d_{va})$ is defined relative to $E_L(d_{va})$, so for spheres $E_s(d_{va}) = 1$, even for particles for which $E_L(d_{va}) < 1$. Note that in the absence of other physical effects that lead to particle loss, $CE(d_{va}) = E_L(d_{va}) * E_s(d_{va}) * E_b(d_{va})$ for a given particle size and type. We can also write $CE = E_L * E_s * E_b$ for the total mass. The limitation of the mass-based definition is that it does not explicitly take into account that CE due to both shape and bounce effects will depend on particle size, as well as phase. Thus, a different mass-based CE may be derived for particles of the same morphology and composition if their size distribution is different. The definitions given here, however, are more precise since they take particle size into account.

Previous d to derive empirica k et al. (2003), r studies perform , NY, which is now b article boun s due to focus able to compare et, so that a large un voided (Zhang culate mass concentr specified for

to depend on the species but not on particle size, although the user can implement the later dependence if this information is available.

2.2. Definition of Non-Sphericity Parameter: Lift Shape Factor

Since spherical particles produce the smallest beam widths after an aerodynamic lens and non-spherical particles result in broader beams, we can define a surrogate non-sphericity parameter, ψ, that we will call the lift shape factor, as:

where $\sigma_{sph}^{d_{va}}$ is the beam width (given as standard deviation of the 2D Gaussian distribution) for a sphere of a given vacuum aerodynamic diameter, $\sigma_{P}^{d_{va}}$ and is the beam width for the particle of interest. It is necessary to compare particles of the same d_{va} since focusing is also known to depend on size (Zhang et al. 2004c). Very little is known at present about the relationship between ψ and the physical particle shape (as determined by microscopy techniques), or between ψ and other parameters capturing the effect of non-sphericity such as the dynamic shape factor χ, or the Jayne shape factor S (DeCarlo et al. 2004). The dynamic shape factor captures the effect of non-sphericity on drag forces on a particle moving in a fluid, and plays a critical role in the interpretation of many particle sizing techniques (DeCarlo et al. 2004).

Only irregular particles experience forces perpendicular to the direction of gas motion ("lift" forces) (Liu et al. 1995a), while for spherical particles lift forces are zero. Given the related physical effects giving rise to χ and ψ (aerodynamic forces and inertia), the ease with which the measurement of ψ can be performed with the beam width probe describe mic shape factor, fu rapid approxir urrogate. The dyn the Reynolds particle orient end on the sam d operating pressure

2.3. Pa

In this se ne beam. In

attenuation caused by the probe. The particle beam is close to a point source at the exit of the lens (~100 μ m diameter, (Heberlein et al. 2001)). Under the high vacuum conditions inside the AMS there are no significant forces, other than a small effect of gravity (DeCarlo et al. 2004) acting on the particles. Thus, we assume that as the particles travel in the vacuum chamber the lateral spread of the particle beam in the direction perpendicular to its travel (“beam width”) increases linearly with the distance traveled. Alternatively, the size of a particle beam can be described by the solid angle it fills, arbitrarily defined as the solid angle encompassing a certain fraction of the beam density, such as 90% of the particle concentration (Kane and Johnston 2000), or the beam standard deviation. We will use the latter definition here. The cone defined by the center point of the nozzle at the exit of the lens and the beam dimensions at the vaporizer, having base radius σ, base area A, and height L (the particle flight length) in the limit of small angles will define a solid angle (Serway 1996):

which can be rearranged to express the dependence of the beam width on the flight distance as:

Note that Equation' (Equation 2) is an approximation to the definition of solid angle. It assumes the base of the cone to be a flat circle (of radius σ), whereas the rigorous definition uses the slightly different area of a sector of a sphere (of radius L) on to which the circle is inscribed. All solid angles discussed here are very small, and the error is negligible.

We will u ath at which a given zer location. Jayne et ms, the shape of elative to the cent n distribut

We revis

For our m can be represer igure 2a). With this article per

decreases monotonically with distance from it, but it does not depend on the azimuthal angle. The equation that describes a 2-D (circular) Gaussian distribution is:

where x and y are the positions along the plane of the distribution, x_0 and y_0 are the coordinates of the center of the distribution in that plane, and σ is the standard deviation. Table 2 shows the fraction of the probability encompassed by 1-D and 2-D Gaussian distributions for different multiples of σ around the center point. Here we will assume that the particle distributions are centered on the axis defined by the lens and the center of the vaporizer (i.e., $x_0 = y_0 = 0$), and thus the only parameter needed to characterize a circular 2-D Gaussian distribution is σ, which we refer to as the particle beam width, and which will depend on the distance from the exit of the lens. We always use the symbol σ with a subscript that identifies the AMS chamber length, and a second subscript for the distance between the lens exit and the position of the beam width measurements.

FIG. 2 Physical depiction of a 2-Dimensional Gaussian (2DG) distribution plot. (a) Particle intensity (particles/cm^2) and probability density function (PDF) at any one distance from the lens exit is assumed to follow this 2-D Gaussian, and drop off radially outward from the center axis. (b) Attenuation density function, which is the 1-D PDF obtained as the partial integral of the 2-D Gaussian PDF for a given value of x along the y-axis, for all the values of y comprised by the vaporizer. The areas under each curve are normalized to one another. (c) Radial density function, which is the 1-D integrated probability-density function (PDF) for all azimuthal angles, θ, around a circle for a 2-D Gaussian[illegible] (d) Cumulat[illegible]ibutions shown in[illegible] impact the vaporize[illegible]iameter. Note tha[illegible]izer for larger b[illegible] graph gives direc[illegible]

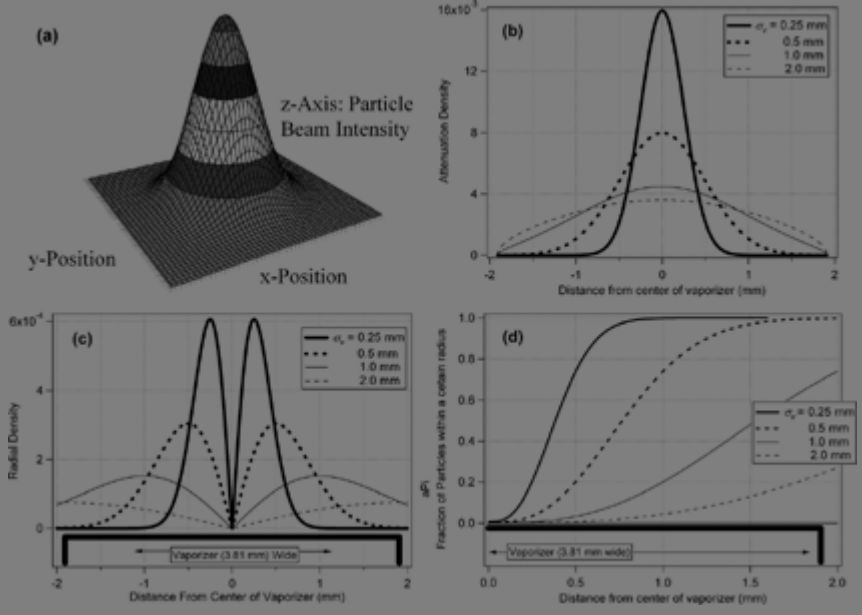

Display full size

TABLE 2 Percentage of the area or volume under 1-D and 2-D Gaussian distributions, respectively, for all independent variable values closer to the mean than different multiples of the standard deviation, σ. 2.35σ (2 · 1.17σ) corresponds to the full-width-half-maximum value (FWHM) for both 1-D and 2-D Gaussian distributions

Download CSV Display Table

Figure 2b shows the one-dimensional PDF (a(x)) obtained by integrating the 2D distribution along its y-axis, but only for those values of y that are inside the vaporizer, and renormalizing by the total area so that a(x) is a proper PDF, i.e. $\int_{x_{min}}^{x_{max}} a(x)\,dx = 1$.

where r AMS designs) lly it can be thought he vaporizer bein ained with an infini integral of a(x) betw ill impact the vapo om the particle

In this article

Figure 2c shows a different 1D PDF (b(r)) which is only a function of the radial coordinate, and that we will refer to as the radial density. b(r) is obtained by integrating the volume under the 2D Gaussian curve for all azimuthal angles, θ .

An additional integral of b(r) over the radial coordinate directly yields probabilities, and thus the total area under each curve in the graph is the same, as in the previous case. The area between two radii is the fraction of particles that hit the vaporizer between those two radii for all azimuthal angles θ. Note that the peak in particle radial density is located one σ_v away from the center. Figure 2c also shows that for σ_v values less than 0.5 mm, the radial density drops to very small values before reaching the edge of the AMS vaporizer. This indicates that for particle beams which can be characterized by $\sigma_v < 0.5$ mm (well-focused particles), E_s will be ~ 100%. Figure 2d is an integration of Figure 2c (B(R)), representing the total percentage of particles impacting the vaporizer to the inside of circles with a given radius R.

Again, for $\sigma_v < 0.5$ mm, all particles will impact the vaporizer, but as σ_v increases, the integrated particle density in the area of the vaporizer can be less than 100%, indicating that the shape-related collection efficiency is below 100%.

While Ω is conserved for a given particle beam under all instrument configurations and particle flight distances, the particle beam width increases linearly with the particle flight distance (Equation 3). The horizontal position of reference (e.g., at the vaporizer, or at the BWP), therefore, must be stated. Since the beam width is the physically meaningful parameter for calculating attenuation by a beam width probe or collection by a vap ripts that unequiv en Ω and σ. Table 3 s lengths. Figure 1 ts the relevant all discu the 255- series ameters to characte e beam width at ” chamber, and v re n the plane of the BW nitions for

TABLE 3 Notation for beam width, σ, must be referenced to a particular particle flight length (AMS chamber configuration) and plane of reference in order to be meaningful. The table defines the four combinations used in this paper

Download CSV Display Table

Note that the 2-D Gaussian assumption would fail if the lens is not well-aligned, and particles are lost via impaction with one of the skimmers inside the instrument. Under these conditions (arising from user error) the shape of the beam could be very different from that predicted by the model. Also note that the total flight length in the AMS is different from the flight length used in the AMS calibration of particle velocity vs. particle size (Jayne et al. 2000). The latter is the distance from the particle chopper to the vaporizer (395 mm), since that is the length that corresponds to the measured particle time-of-flight, rather than from the lens exit to the vaporizer.

2.4. Beam Width Probe Design

A beam width probe was designed and implemented to provide a real-time quantitative measurement of the width of the particle beam in the AMS, and thus enable the estimation of ψ and E_s for the particles being sampled. Figure 3 shows a schematic diagram of the probe set-up together with the vaporizer from two different perspectives. Two probes have been developed. The first prototype uses a servo motor (HiTech, HS-81) to position the probe (a wire or ribbon of known dimension) across the path of t 0 μ m. A second, 5) was built for impr ticle time-of-flight 1). When the probe is signal attenua art of the parti eaching the vaporize or each chemica f-flight region w) there are very few etween a 100 nm and

In this article

are intercepted by the probe will not reach the vaporizer. Thus, the BWP shades a certain fraction of the vaporizer and reduces the AMS signal by the fraction of particles in this shaded area. The BWP has also become very useful for determining alignment of the lens. Instead of moving the lens slowly back and forth, and watching for a resultant drop in signal when the beam was pushed beyond the sides of vaporizer, the BWP can be quickly moved back and forth to determine the horizontal placement of the particle beam focus. With the current BWP design, however, this works only in the horizontal direction. For vertical alignment the BWP needs to be rotated 90 degrees, which requires breaking the vacuum, or the “classical” alignment procedure by lens aiming is still necessary.

FIG. 3 Schematic diagram of the beam-width probe from two perpendicular views. The particle beam is projected from the lens exit towards the vaporizer, and it broadens as it moves down the vacuum chamber. Particles will ideally follow a narrow trajectory (spherical particles) and impact the vaporizer. Some particles may follow trajectories that will miss the vaporizer surface (irregular shapes). The beam width probe is positioned selectively in positions that either partially block particles moving towards the vaporizer, or in the ‘out’ position to obtain un-attenuated measurements. This diagram is not drawn to scale.

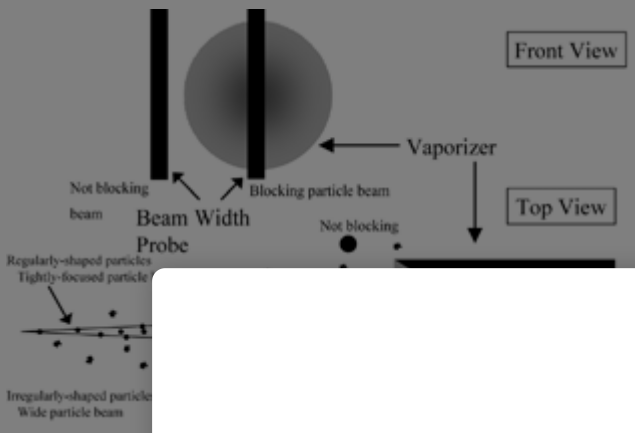

Display ful

2.5. Re

By pre ervals as describe on, the attenuat -D Gaussian particle robe position curves. T

In this article

transmission curve as a function of wire position, wire diameter and particle beam width. The model assumes that the particle beam density as a function of radial position is well represented by a circular two-dimensional Gaussian distribution, as described above. The model is computed in two steps. First the vaporizer is discretized along the x-axis, and the integral of the particle beam density function for a small interval of x and all values of y inside the vaporizer (the “attenuation density” described above, a(x), see Equation 7) are calculated for a series of particle beam widths. The attenuation created by a given wire as it is set to block certain x positions is just the integral of the attenuation density of the blocked x positions, since the attenuation density is a PDF. Note that the total detectable signal could be smaller than the total beam intensity if $E_s < 100\%$ (i.e., beam width > diameter of the vaporizer).

2.6. Field Operation of the BWP

For normal operation of the probe during a field or laboratory study, several wire positions are chosen, e.g., eight total steps, including the center, three on each side of the center (but within the vaporizer cross section, “partially blocking” positions), and one position completely outside of the vaporizer (“out” position). The probe is moved to each successive position in one direction, with the “out” position interleaved in time between each “partially blocking” position. Data taken during the periods when the probe is completely outside the beam and no attenuation occurs allows for a total mass trend to be established for ambient monitoring and comparison with other instrumentation. The number of positions should be chosen to provide enough attenuation, measured as a function of wire position, to constrain the data fit to the model cu g” steps, with the cle time (out → partia nges in the particle o the average n, the total cycle ti the time scale attenuation profile c

Under n e is often configur s. For example with the

the vaporizer center. This longitudinally covers the center 3.5 mm of the vaporizer, and contains most of the information. Using seven steps, interleaved with seven non-blocking positions amounts to a 14-minute cycle with 1-minute averaging at each position. For applications when time resolution is critical, such as when sampling from aircraft, it is recommended that only two positions (center and non-blocking) will be selected and applied with a small duty cycle (~ 10% of the time in the blocking position) in conjunction with the new “Jump Mass Spectrum” mode (i.e., selective ion monitoring) of the AMS, so as to minimize the loss of normal mode data and maximize the temporal resolution of the ψ and E_s determinations.

3. RESULTS AND DISCUSSION

3.1. Particle Collection Efficiency

The vaporizer diameter and its distance from the lens exit define a cone of a certain solid angle. For the long-chamber AMS length of 450 mm from lens exit to vaporizer, the solid angle of collection is 5.63×10^{-5} sr (Table 1). Provided that the center of the particle beam is centered on the vaporizer, particles that follow a trajectory within this cone will impact the vaporizer. At this position the relative number of particles (probability density) at each location radially outward from the beam center, and therefore at each solid angle, is only a function of the particle beam width at the vaporizer (σ_v). The vaporizer collection efficiency due to shape (E_s) is then simply a function of the particle beam width at the vaporizer relative to the vaporizer diameter, or altern ed to the vaporize am calculate is the same for all ch zer is used. Beam wi nust first be scale

FIG. 4 Va of the width of the pa bottom axis, and termined beam wi cid) and very irre

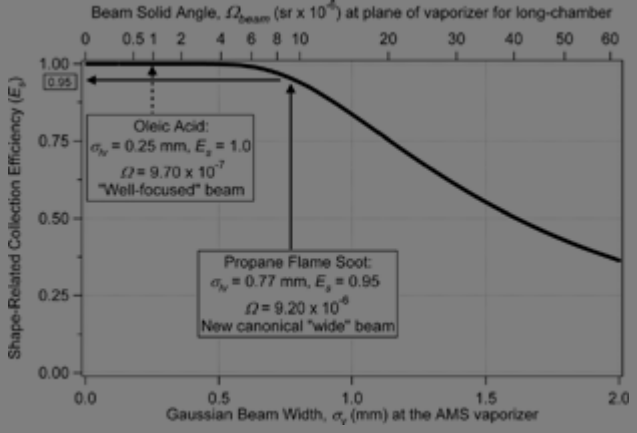

Display full size

E_s remains 100% for narrow beams (small σ_v), and until the beam becomes wide enough so that a significant fraction of its tail misses the vaporizer surface. At $\sigma_v \sim 0.625$ mm ($\Omega \sim 5.63 \times 10^{-5}$ sr for the AMS long chamber) E_s drops below 99%. For very irregular soot particles that have a $\sigma_{lv} = 0.77$ mm (Slowik et al. 2004) E_s will be approximately 95% for the AMS long chamber. Reducing the chamber length by 10 cm would reduce the beam width at the vaporizer, σ_{sv} to 0.59 mm, and thus increase E_s for these less well focused soot particles to slightly more than 99%. Partially as a consequence of these results, Aerodyne Research has produced a chamber with a particle flight path approximately 10 cm shorter (referred to here as the “short” chamber, 215-series design). This increase in E_s can be accomplished with less than proportional loss in particle size resolution (Jimenez et al. 2001). As the particle flight length decreases, the time-of-flight for the largest particle to be sampled by the AMS in a given experiment (d_{max}) also decreases. This allows the increase of the chopper frequency so that a chopper period still allows a particle with $d_{va} = d_{max}$ to arrive before th y reduces the chop e time-of-flight (PT tainty stays constant of the AMS is partic end on chamb rger unce resolution.

3.2. Be

Through pected beam wi particles

section. Liquid oleic acid particles with mean d_{va} of 320 nm show $\sigma_{lv} = 0.13$ mm. Slowik et al. (2004) show that very irregular soot particles generated by a propane flame burner have $\sigma_{lv} = 0.77$ mm, defining the upper bound of expected beam widths. Figures 5a and 5b show the modeled results of the particle beam attenuation versus probe position for probe diameters of 0.39 mm and 1.09 mm, which will be shown later to be the optimal probes for the above-defined canonical narrow and wide beams, respectively. Again, all results presented refer to the "long" AMS chamber. Each curve shows the percentage beam transmission (normalized to an unattenuated beam) as the probe is moved across to block a fraction of the vaporizer. For an extremely narrow beam ($\sigma_{lv} = 0.01$ mm), particle beam attenuation is predicted only when the wire intersects the center of the vaporizer, where the beam is focused, using probes of the above mentioned diameters. Note that this beam width is unrealistically small given current aerodynamic lens technology, as the lowest beam widths for spherical particles for this flight length are of the order of $\sigma_{lv} = 0.13-0.25$ mm. The limit of a very narrow beam is shown in Figure 5, however, because it provides an asymptotic result and helps in understanding the results of the model. The width of the attenuated section is simply the width of the wire as projected onto the vaporizer plane. Note that the "shadow" of the wire broadens slightly due to the constancy of the solid angle, as defined earlier (Equation 3).

FIG. 5 (a) Particle beam transmission curves for a BWP with a 0.39 mm wire (nearly optimal for well-focused beams) for the long AMS chamber. The different lines show the attenuation of particle beam vs. BWP position for several particle beam widths (σ_{lv}). (b) Similar curves for a 1.09 mm wire probe, showing broader and deeper attenuation for each [illegible] flame soot particles [illegible] poorly focused [illegible]

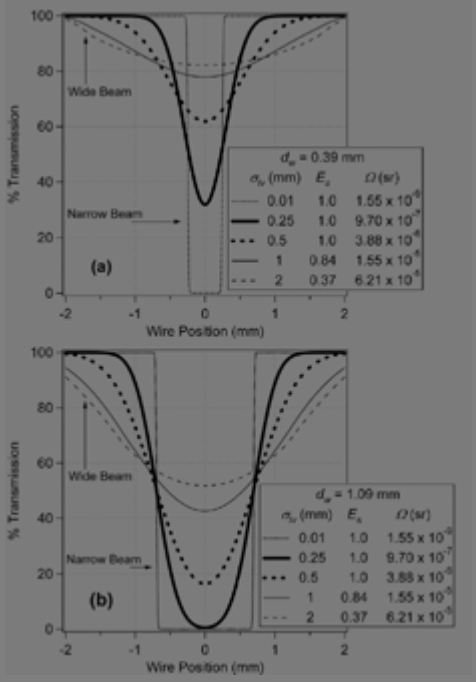

Display full size

For an extremely broad (nearly uniform) beam of particles the attenuation is simply the geometric area of the vaporizer that the wire probe is blocking (because the particle probability density is nearly uniform across the width of the vaporizer). For particle beam widths of intermediate values and realistic proportion, the percentage of particles blocked is the product of the geometric area the probe shadow casts on the vaporizer with the relative concentration of particles (the probability density given by the Gaussian distribution) for those locations. For a given geometry and wire diameter, each beam width gives rise to a unique attenuation curve. Optimal probe geometries will be discussed below.

3.3. Pa

Once da s a function of wire p gorously determi nation, the data sho With this meth d input to the r idth values. The moc when compare

In many on in the detailed nalysis, the

"1DG" parameterization achieves two benefits: (1) experimental data can be easily and quickly analyzed inter-compared based on σ_{1DG}, the standard deviation of the 1DG fit curve, for first-order data analysis, and (2) imperfections in the lens alignment can be removed from BWP analysis, because the Gaussian fit will automatically "re-center" the data to a better estimate of the true horizontal beam center, which in general will not be exactly the same as the vaporizer center. This re-centering can be used to define a horizontal offset of the beam center for the modeling of σ_{lv} for misaligned particle beams. Figure 6 shows the relationship between σ_{lv} and σ_{1DG} for four different BWP diameters. For $\sigma_{lv} > d_w/2$, σ_{1DG} is a reasonable approximation to σ_{lv}. This rule of thumb allows a quick first-order analysis and inter-comparison of experimental data. Note that the validity of the 2DG assumption is not directly related to the results of the 1DG fit. The validity of the 1DG parameterization is further discussed in the probe optimization section below.

FIG. 6 Relationship between the beam width approximated by a 1-dimensional Gaussian data fit (σ_{1DG}) and the more rigorous value of beam width determined by the model output (σ_{lv}) for four BWP sizes. Note that when using Igor Pro (Wavemetrics, Inc.) the Gaussian fit "width" parameter returned is $\frac{\sqrt{2}}{2}$

σ_{1DG}.

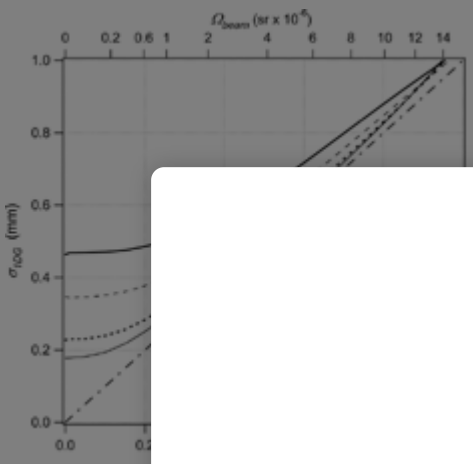

3.4. Mo a

We perfo ne assumpt distribution. Beam wi ng pure-

St. Paul, MN), and then size-selecting particles with a differential mobility analyzer (DMA, TSI model 3081, St. Paul, MN). All solutions were prepared by dissolving the species in HPLC-grade water, with the exception that oleic acid was dissolved in HPLC-grade ethanol. The aerosol was dried by three silica-gel diffusion driers in series, and the humidity after the driers was monitored with a relative humidity probe (Vaisala Humitter 50Y, Helsinki, Finland). RH was kept under 25% throughout all experiments. Then the aerosol was introduced into the AMS inlet, where the particles were focused onto a narrow beam that was directed onto the AMS vaporizer. The beam width was measured as the BWP was walked across the vaporizer in very small steps (22 total positions).

Analysis was performed using the signal from species-dependent fragment ions (NH_4NO_3: m/z 16, 17, 30, and 46; $(NH_4)_2SO_4$: m/z 16, 17, 48, and 64; Oleic Acid: m/z 43 and 57) from singly-charged particles exiting the DMA, with the exception that 550 nm oleic acid data were taken from doubly-charged particles and using only m/z 43. Two monodisperse sizes were used for each species, approximately 110 nm and 320 nm, in addition to 550 nm oleic acid. Particle transmission plots for these data are shown in Figure 7. The beam profiles of all species and particle sizes are reasonably well captured by the results of the BWP computer model described above, which indicates that the two-dimensional circular Gaussian approximation for the particle probability density is reasonable. Note that the particle beam focus points with a real lens are slightly size-dependent, due to imperfections in lens machining.

FIG. 7 Pure, monodisperse particle beam profiles, shown ± the standard error of the mean. D roughput lens sam .5 mm wire probe. 2 th high spatial r σ_{lv} and Ω values fo ork, and are listed in outputs fit to th NO_3 particles Acid particles

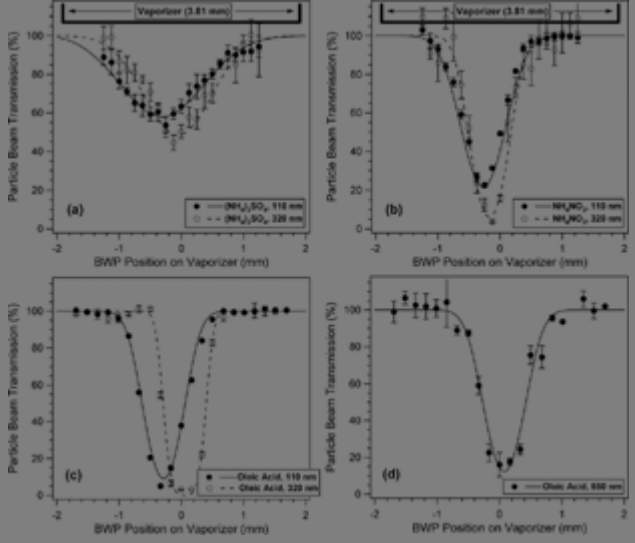

Display full size

TABLE 4 A summary of particle beam width measurements published by several research groups, and those from this work. Since each group presents results in a different format and for different particle flight distances, the reported values have all been scaled to the standard deviation of a Gaussian beam at the particle flight distance of the long-chamber AMS (450 mm), and to the solid angle that this area would encompass. Note that the lens types used for AMS instruments are similar, but not identical to the Liu et al. lens. Ψ has also been calculated when appropriate, as described in the text

Display Table

The bea d particles (where E ticle beam width m earch groups. d these data were all e beam widths designs and oper e summar 08) use a different aller lens orifices. hreiner data have be Liu-style lenses h non-

In this article

PSLs to be slightly non-spherical. This shows that spherical particles appear to have size-dependent focusing, as expected. Very small particles (40 nm) produce broad beams due to the limitations in the focusing of the aerodynamic lens and as a result of particle Brownian motion. Large particles (> 500 nm) do not focus very well due to their high inertia, with the consequence that particles only partially follow the gas streamlines in the lens that causes the particle focusing. Intermediate sizes of spherical particles (300 nm) show optimal focusing (Zhang et al. 2004c). Non-spherical particles are generally less well focused than spherical ones, and focusing is different for the various species (due to their different shapes).

FIG. 8 (a) Literature summary of beam width measurements from a number of research groups. Note that the Schreiner papers employ a high-pressure lens, and have been plotted on the right axis. These lenses may focus particles differently than the ones described in the other five papers, which all use the Liu-style lens (left axis). Data from instruments using the Liu lens are divided into mostly spherical particle types (left group) sorted by size, and non-spherical particles (center group) sorted by species. The Katrib 2005 data was taken from textual references of beam width data, as well as from Figure 2 of that paper, which was then analyzed via the methods described in this paper. Note that PSLs are considered slightly non-spherical based on the results of Katrib et al. (2005). (b) Ψ values have been calculated for corresponding beam width data. Each non-spherical particle σ_{lv} was divided by the σ_{lv} for a spherical particle of similar size, from the same publication.

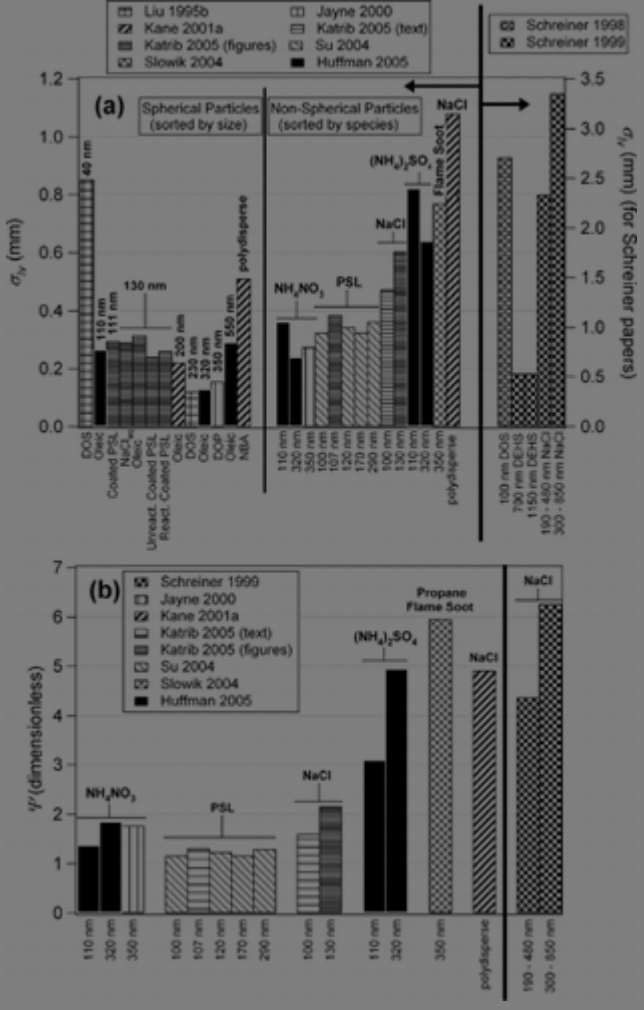

Display full size

Figure 8b relates this shape information as the lift-shape factor, ψ, introduced here (Equation 1) and showing the effect of shape on particle focusing. Each non-spherical data point from Figure 8a was referenced to a corresponding spherical data point of similar size from the same publication. Su et al. (2004) did not record a spherical data point, and so the average of the 130-nm data points from Katrib et al. (2005) was used for refer and so the 320-nm

The prec rticle size-depende l in the particle osol was bloc osition of the bea ees, indicatin nd Matthew 2004). T ains why the particle y monodis r studies

Computer code for rigorously analyzing laboratory and field data using the 2-dimensional model is available at: http://cires.colorado.edu/jimenez-group/SI/.

3.5. Field Results

Allan et al. (2004) suggest that some ambient non-spherical particles may also be collected with less than 100% efficiency by the AMS. Although this effect was previously attributed to very wide ambient particle beams, it has recently been shown that most of the reduced particle collection efficiency is due, rather, to particle bounce at the vaporizer (Onasch 2004). With the results of the model discussed here, it is now believed that reduced collection of ambient particles due to very wide particle beams is not a significant problem for the AMS. Salcedo et al. (2005), Weimer et al. (2005) and Delia (2004) all conclude that $E_s \sim 1$ for ambient particles studied in the field in Mexico City, New York City, and Duke Forest, North Carolina respectively.

3.6. Optimization of the Wire Probe Width

The BWP can be used to measure the particle beam width and estimate the lift shape factor (ψ) and shape-related collection efficiency (E_s) in near real time. By running the model for a variety of BWP dimensions (diameters, d_w), we can determine optimal probe dimensions with maximum sensitivity to measure E_s or ψ (i.e., to have the lowest possible uncertainty on the measured E_s or ψ). The optimum wire width will depend on the width of the beam under study, and thus a compromise should be made, since the probe is inside the vacuum chamber and cannot be changed quickly under varying ambient conditions.

For succ tion at each point inc to provide a precise b nange in attenuat maximized. S_σ is de

and has at the central p

The prec tenuation signal w

and is dimensionless. Conceptually, maximizing S_σ by choosing the optimum d_w is equivalent to maximizing the separation between the curves, such as those in Figure 5, representing the differences in attenuation caused by small changes in σ_{lv}. For discussion of the wire optimization towards narrow beams, a beam width of 0.25 mm was chosen to represent reasonably well focused, nearly spherical particles. While the value of $\sigma_{lv} = 0.13$ mm was shown to be optimal for the particles exhibiting the best possible focus (Figure 7), the larger value is more realistic for well-focused ambient particles, and has been taken as the approximate average of the spherical data points from other studies (Figure 8a). Note that E_s remains unity in each case.

The first step in this approach is illustrated in Figure 9, which shows the difference between two close values of σ_{lv} for several d_w. Examples for narrow and wide particle beams are shown in Figures 9a and 9b, respectively. The absolute value of the "difference curves" in the plot describes how far the two absolute attenuation curves (as in Figure 5a) are separated from one another, and therefore how much sensitivity is achieved at each of the probe positions. The center position has the largest sensitivity for most cases, but as d_w/σ_{lv} increases, the point of maximum sensitivity moves away from the center and towards the vaporizer edges. We will focus on the attenuation at the center position for the rest of this analysis, since this position will have the maximum attenuation for most cases of interest.

FIG. 9 Difference curves between the modeled transmission curves (similar to Figure 5) for two close particle beam widths for a variety of probe diameters. The difference from zero in t urement for each wir = 0.22 mm and 0.23 ns. (b) Differen ensitivity towards nter, except when d

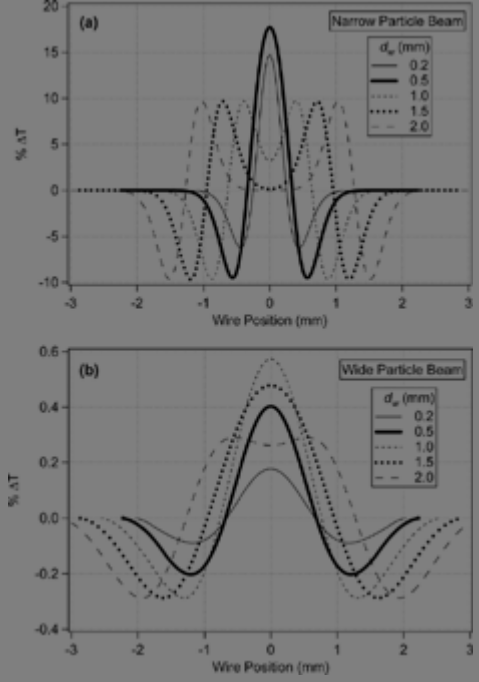

Display full size

The mathematical procedure for estimating the sensitivity is summarized in Figure 10a. Figure 10a shows $da_c/d\sigma_{lv}$, $d\sigma_{lv}/dE_s$, and da_c/dE_s for $d_w = 0.5$ mm. $da_c/d\sigma_{lv}$ was calculated directly from the model by computing the difference curves (as in Fig. 9) in small $\Delta\sigma_{lv}$ intervals (for a given d_w), and then estimating the derivative numerically as $\Delta a_c/\Delta\sigma_{lv}$. This particular wire ($d_w = 0.5$ mm) is most sensitive for the measurement of beam width around $\sigma_{lv} \approx 0.23$ mm, but maintains some sensitivity for much larger beam widths. The sensitivity to E_s can be computed by using the following mathematical relationship:

FIG. 10 Plots representing the sensitivity analysis for the wire-based beam width probe. (a) Summary for d_w = 0.5 mm, showing that da_c/dE_s can be found as the product of the othe… of BWP sensitivi… nd beam width. M… neter and beam siz… to σ_{lv} fits a line of sl… $_v$ = 0.6 mm. (c) In… m the model produc… since E_s does not… vity is the same as…

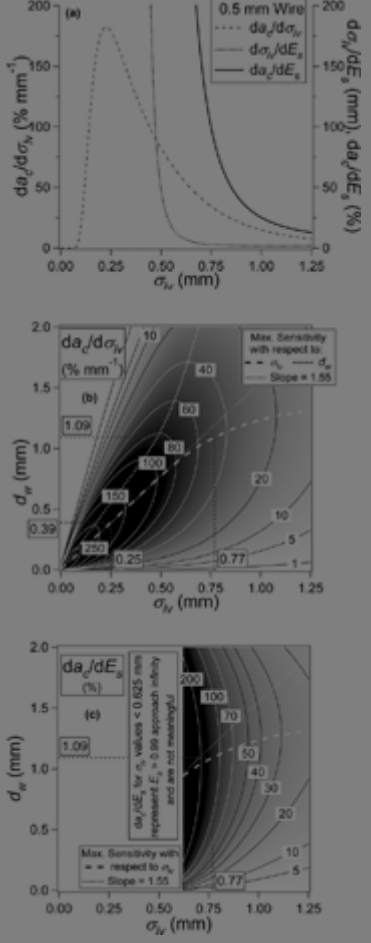

Display full size

The term $d\sigma_{lv}/dE_s$ can be easily computed as the numerical approximation to the derivative of the curve in Figure 4.

Figure 10b summarizes S_σ for all particle beam and wire probe diameters. An optimal d_w can be chosen for every σ_{lv}, but there is a range of d_w that provides significant sensitivity for a given σ_{lv}. Curves joining the points of maximum S_σ with respect to σ_{lv} and d_w a… ct to d_w ($S_{\sigma(max,d)}$) w… rection, and plotting … $\sigma_{(max,\sigma)}$) was calc… due to the slope an… imal d_w can be c… linear approx… arger σ_{lv} the line over… differences between…) is $d_w \sim$ 0.39 mm… ~ 0.77 mm) the optim… ensitivity

In this article

Figure 10c shows the sensitivity to E_s (S_{Es}). Note that $E_s > 0.99$ until $\sigma_{lv} > 0.625$ mm. For smaller σ_{lv} the term $d\sigma_s/dE_s$ in Equation 12 can be very large since E_s changes very little as σ_{lv} changes, resulting in very large values of da/dE_s. However, these have no practical significance since $E_s \sim 1$, and thus they are not shown in the figure. For $\sigma_{lv} > 0.625$ mm there is an optimum d_w for determining E_s (maximum S_{Es}). The curve of maximum S_σ is the same as the curve of maximum S_{Es}, because the two sensitivities are related by a factor that does not depend on σ_{lv} (Equation 12).

Figure 11 provides an alternative representation for the information provided by the BWP, which can be especially useful to guide in choosing the additional probe positions (other than the center) to be used for field studies. Figure 11a uses $d_w = 1.0$ mm, which is close to optimal for wide beams, and Figure 11b uses $d_w = 0.39$ mm, which is optimal for narrow beams. Curves in the figure represent the change in signal attenuation (as σ_{lv} changes) for a different physical location of the BWP, differing by full or $^1/_2$ diameters of the wire for each position (full-, half-step) of the probe. The bottom curve for each figure probes the center of the particle beam, where particle density, and resultant signal attenuation, is highest. Additional positions shown in the figure represent the attenuation at other probe locations. The areas of each curve with steeper slopes provide better sensitivity for beams of those σ_{lv}, because small changes in σ_{lv} produce significant changes in transmission. Areas that are nearly flat provide very little information about beam width because large changes in σ_{lv} cause only a small difference in transmission. For example a change in beam width between $\sigma_{lv} = 0.5$ and 0.75 mm in Figure 11a results in an easily detectable 18% change in absolute transmission at the center position, giving an average nominal sensitivity of 71%/mm

produces a harder t

sitivity of 4.4%/mr

mal informat

where E_s is less thar

n particle shap

L. This figure also

position.

FIG. 11 F

al positions of the w

hile flat regions

e. (a) Curves f

optimal for

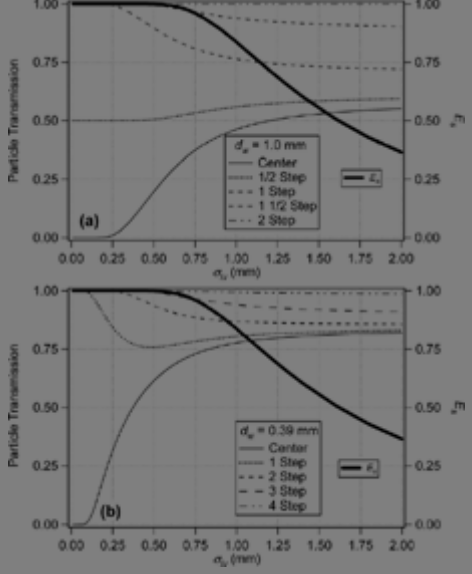

Display full size

3.7. Results for AMS Short Chamber

As mentioned, these results are given for the long-chamber AMS, but can be extended to any other AMS chamber design, because for the same lens and particle type, the solid angle of the particle beam will be the same. Thus, the beam width at the vaporizer will be smaller in the short chamber by the ratio of the particle flight distances (Equation 3), i.e., $\sigma_{sv} = 0.77 \cdot \sigma_{lv}$. The width of the projection of the wire probe on the vaporizer surface will be $450/353 \cdot d_w$ for the long chamber, and $348/251 \cdot d_w$ for the short chamber. For the wire probe to block the same linear angle of particles, the width of the wire must be reduced according to the ratio the ratio of distances from lens to BWP. Thus, $d_{ws} = 0.71 \cdot d_{wl}$. Since the optimum wire for the long chamber was $d_{wl,opt} = 1.55 \cdot \sigma_{lv}$, the optimum wire for the short chamber can then be estimated as $d_{ws,opt} = 1.43 \cdot$ [illegible] monical narrow ([illegible] 44 mm represer [illegible] t studies.

3.8. Alt [illegible]

In addi [illegible] geometries show [illegible] etely blocks the parti [illegible] 'knife-edge' model u [illegible] oints to the left of th [illegible] he vaporizer ($d_w >$ d [illegible] d on the

Commercial laser alignment components may be available to implement this latter design.

FIG. 12 Schematics of four alternative beam-width probe geometries (black) superimposed on the vaporizer (gray), including the wire probe geometry discussed so far, and the geometry of movement modeled for each.

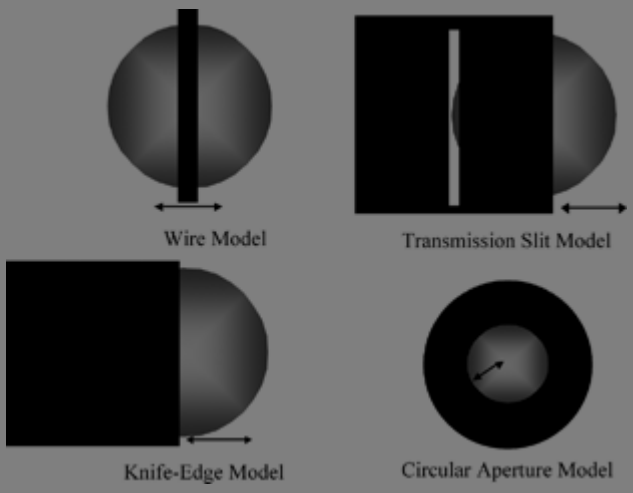

Display full size

The transmission slit is directly related to the wire probe. When the slit width and wire width are matched, the slit probe produces attenuation curves exactly the inverse of the wire probe model of the same width. Thus, there is not a major advantage of the slit compared to the wire probe, and the wire is preferred due to simpler construction and alignment. The knife-edge probe acts as an infinitely thick wire, and as discussed above it provides sub-optimal information as compared to wire probes with smaller d_w (see Figures 9, 10, 11), so it will not be discussed further. Using a second wire or knife-edge probe ro article beam in the ot ay not be perfectl uming a circular

Figure 1 ius for the varia n a similar curve to beam width (S ference in signal tr σ_{lv}. Figure 1 .02, as example e), as well

In this article

optimal wire for each σ_{lv}. Note that this would mean changing the wire for optimal results in different σ_{lv} regions, and would therefore be impractical, but is shown for reference. The gain in sensitivity is shown on the right axis of Figure 13c. The circular aperture shows an increase in sensitivity by approximately 50–75% over the optimal wire at any given beam width, and considerably more for any one chosen wire. Thus, it would be desirable to use this probe instead of the wire-based probe. The circular aperture probe, however, may be difficult to implement in a high vacuum environment, and would be considerably more costly. Beam alignment would also become even more critical to the operation of the probe, and the complexities associated with different focusing beam center positions for different particle sizes (as described above) would be difficult to deconvolve from the data. On the other hand, the wire probe is by design "self-aligning." For these reasons, we currently advise the use of a wire-based probe with a wire diameter of 0.62 mm in the long AMS chamber (0.44 mm in the short chamber) in order to provide optimum sensitivity for measurement of σ_{lv} (and ψ and E_s) for ambient particles.

FIG. 13 (a) Transmission curve summary for the mathematical model of the circular aperture beam width probe. The radius of the aperture opening is the operational variable that can be changed, conceptually similar to the position of the wire probe. As the opening increases in size, the percentage of particle transmission increases as a function of the width of the particle beam (displayed on different lines). (b) The difference in attenuation signal (Δa_c) when the beam width changes is shown for two pairs of beam sizes as a function of aperture opening position. This mathematical difference is an intermediate step in determining the sensitivity ($da_c/d\sigma_{lv}$), values in the third
erture
probe, a
timal wire
probe us
probe, and
the circu

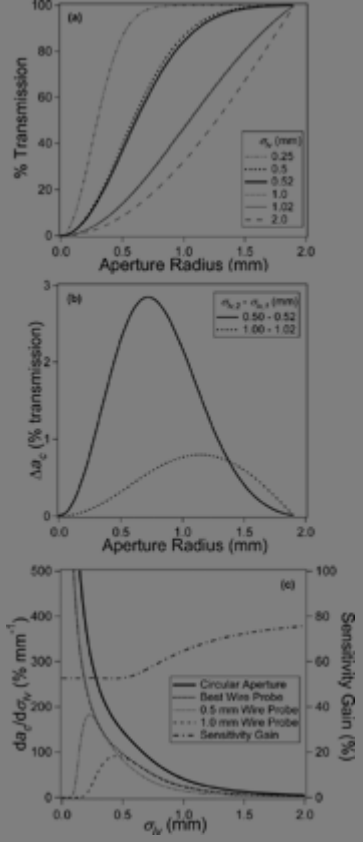

Display full size

3.9. Estimation of Relative E_s for Other Particle Beam Instrument Geometries

The larger beam widths for non-spherical particles as compared to spherical ones can result in a potential detection bias for any instrument that uses aerodynamic lens inlets, with the spherical particles being detected more efficiently, and thus leading to a relative undercounting of the non-spherical ones. With the measurements performed with the AMS for various particle types and the model presented in this paper, we are in a positio er instrume metry of the particle slightly differen MS have similar b tical estima r four com articles are detecte ower distribut collection efficienc angle. Vertical e (Figure 8,

ambient particles as seen in Mexico City (Salcedo et al. 2005). Figure 14b shows the relative instrument detection bias (with respect to spheres) as a function of solid angle of collection for the particle types shown in Figure 14a. As the solid angle of collection decreases (either because of smaller detector geometry, or longer flight path) the relative collection bias increases. For example the estimated detection bias to flame soot for the short-chamber AMS is approximately 1.007 (for $\Omega_{collection} = 9.31 \times 10^{-5}$), while the bias for the long-chamber AMS is 1.05 (for $\Omega_{collection} = 5.63 \times 10^{-5}$). The estimated detection bias to flame soot (and solid angle of collection) for laser ablation designs #1 and #2, are 2.22 (for $\Omega_{collection} = 1.10 \times 10^{-5}$) and 6.38 (for $\Omega_{collection} = 3.14 \times 10^{-6}$), respectively. Zelenyuk and Imre (2005) have recently reported observing this shape bias with their laser-ablation mass spectrometer.

FIG. 14 Estimated relative detection bias between spherical particles and other particles types. (a) Shape-related collection efficiency (measured particle concentration divided by actual concentration) as a function of solid angle of particle beam. Each of four instruments defines a curve. Four laboratory-generated particle types are shown as vertical lines, and dashed region shows range of particle beam sizes observed in MCMA-2003 field campaign in Mexico City (Salcedo et al. 2005). (b) Estimated relative detection bias ($E_{s,\ spheres}/E_{s,irreg}$) between spherical particles and other particle types as a function of solid angle of collection. Each curve shows the relationship for a single particle type, with the dashed region showing the measured range from Mexico City. The points show the estimated biases for four particle MS instruments. Note that these are only predicted values based on the instrument geometry, and the model presented here, and have not been verified experimentally.

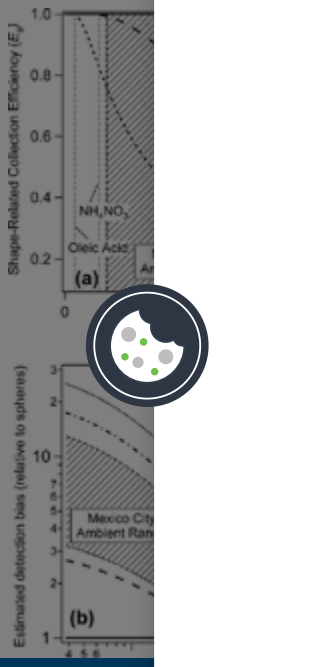

Display full size

This increase in estimated detection bias arises from the fact that laser spot sizes are small, leading to relatively smaller solid angle of detection. The percentage of particles collected from a wide beam, therefore, is also small, and detection is sensitive to the particle beam width. The AMS has an advantage in this regard, because of its relatively large solid angle of collection, due to its large vaporization surface (d_v = 3.81 mm) as compared to typical laser spot sizes.

4. CONCLUSIONS

The use of aerodynamic lens inlets in aerosol mass spectrometers allows for efficient focusing of particles within a given size range, and has revolutionized the ability to analyze ambient particles in real time. Particles exit the lens as a tightly focused beam, but with finite divergence due to imperfect aerodynamic focusing, as well as Brownian motion and lift forces. The latter solely affect non-spherical particles, and so the focusing characteristics of a given particle type can be characterized by a surrogate non-sphericity parameter, ψ, the lift shape factor.

Ideally, all particles exiting the aerodynamic lens used in the AMS will impact onto the vaporizer surface in order to be evaporated and detected. It is important to have a quantitative measurement of the shape-related collection efficiency (E_s) in order to correct the measured mass concentrations for this effect. E_s is defined as the fraction of partic vacuum aerodyn dth probe designe the particle density i was validate percentage of pa vaporizer (as comp of particle beam wi amber AMS designs, han unit efficienc the least focused 0.95). This

is an important conclusion from this work, because prior to the use of this model, it was estimated that collection losses arising from particle shape were significant.

Improvements in E_s for the AMS as a function of reductions in chamber length were estimated with the model. By reducing the distance from the lens exit to the particle vaporizer by 102 mm (450 mm to 348 mm) the E_s of fractal soot particles will increase from approximately 95% to more than 99%.

The model was then used to characterize the signal attenuation as a function of particle beam width for the beam width probe described here, and to optimize the beam width probe for the determination of $\sigma_v(\psi)$ and E_s. The model shows that the optimum wire diameter for very irregular fractal soot particles with the AMS long chamber ($\sigma_{lv} \sim 0.77$ mm) is $d_w \sim 1.09$ mm, while the optimum wire probe diameter for beam width measurement of well-focused beams for nearly spherical particles ($\sigma_{lv} \sim 0.25$ mm) is $d_w \sim 0.39$ mm. An intermediate width of 0.6 mm (0.44 mm in the short chamber) is recommended for general-purpose measurements.

Three other probe geometries were also modeled and compared to the existing wire probe design. A knife-edge design provides sub-optimal sensitivity, while a transmission slit provides an exact inverse of the wire attenuation, but it is more cumbersome to implement. The circular aperture has sensitivity 50–75% greater than for any wire probe, but would also be more difficult to implement and operate reproducibly.

An estimate of particle detection efficiency of several mass spectrometer designs for several pure particle types, as well as for a range of ambient particles was calculated with resp ws that as solid ang and that existing expected collectio

APP

List of te

BWP	

σ	=	standard deviation of Gaussian distribution
σ_{v}	=	particle beam width (one standard deviation) at the vaporizer
σ_{lv}	=	particle beam width at the vaporizer for the long AMS chamber
σ_{sv}	=	particle beam width at the vaporizer for the short AMS chamber
σ_{lw}	=	particle beam width at the BWP for the long AMS chamber
σ_{sw}	=	particle beam width at the BWP for the short AMS chamber
$\sigma^{d_{va}}{}_{p}$	=	particle beam width for a given particle, of a given size
$\sigma^{d_{va}}{}_{sph}$	=	particle beam width for spherical particles, of a given size
σ_{1DG}	=	standard deviation of 1-dimensional Gaussian data fit
L		
L_{l}		
r_{v}		
d_{v}		

d_w	=	wire probe diameter
Ω	=	solid angle
Ω_{beam}	=	solid angle a particle beam encompassed (at 1σ)
$\Omega_{collection}$	=	solid angle of collection for an instrument
ψ	=	lift shape factor
χ	=	dynamic shape factor
S	=	Jayne shape factor
d_{va}	=	vacuum aerodynamic diameter
d_{max}	=	largest particle size to be sampled
CE		
E_b		
E_s		
E_L		

		lens
a_c	=	particle beam attenuation at the center of the beam
S_σ	=	sensitivity of the attenuation signal to a change in beam width
S_{Es}	=	sensitivity to E_s

Acknowledgments

The authors thank Jay Slowik of Boston College for use of propane flame-generated soot data, Dara Salcedo of the Centro de Investigaciones Químicas, Universidad Autónoma del Estado de Morelos, Cuernavaca, Morelos, México for use of ambient Mexico City data, as well as Ann Middlebrook, Dan Murphy and Dan Cizczo of NOAA, Alice Delia of the University of Colorado, James Allan of the University of Manchester, the AMS Users Community, and the Jimenez Research Group for helpful discussions. We also thank NASA Earth System Science (grant NNG04GA67G) and EPA (grant EP-D-04-008) for funding. J. Alex Huffman and Allison Aiken are grateful for NASA Graduate Fellowships (grants NGT5-30516 and NNG04GR06H respectively).

Transmission Efficiency of an Aerodynamic Focusing Lens System: Comparison of Model Calculations and Laboratory Measurements for the Aerodyne Aerosol Mass Spectrometer

Source: Hosted by Utah State University Libraries

Laboratory characterization of an aerosol chemical speciation monitor with PM2.5 measurement capability

Source: Informa UK Limited

A Numerical Characterization of Particle Beam Collimation by an Aerodynamic Lens-Nozzle System: Part I. An Individual Lens or Nozzle

Source: Informa UK Limited

Chemical Analysis of Individual Alkali-Containing Aerosol Particles: Design and Performance of a Surface Ionization Particle Beam Mass Spectrometer

Source: Informa UK Limited

Vapor wall loss of semi-volatile organic compounds in a Teflon chamber

Source: Informa UK Limited

Time- and size-resolved chemical composition of submicron particles in Pittsburgh: Implications for aerosol sources and processes

Source: American Geophysical Union (AGU)

Characterization of the sources and processes of organic and inorganic aerosols in New York city with a high-resolution time-of-flight aerosol mass apectrometer

Source: Copernicus Publications

Collection Efficiencies in an Aerodyne Aerosol Mass Spectrometer as a Function of Pa

Sour

An in study of bi

Sour

Semi nd a R gns

Sou

Dens

Sour

SUBM

Sour

The Pasadena Aerosol Characterization Observatory (PACO): chemical and physical analysis of the Western Los Angeles basin aerosol
Source: Copernicus GmbH
Organic matter and non-refractory aerosol over the remote Southeast Pacific: oceanic and combustion sources
Source: Copernicus Publications
Airborne measurements of the spatial distribution of aerosol chemical composition across Europe and evolution of the organic fraction
Source: Copernicus Publications
Seasonal and diurnal variations of particulate nitrate and organic matter at the IfT research station Melpitz
Source: Copernicus GmbH
Focusing of Aerosols into a Particle Beam at Pressures from 10 to 150 Torr
Source: Informa UK Limited
From Agglomerates of Spheres to Irregularly Shaped Particles: Determination of Dynamic Shape Factors from Measurements of Mobility and Vacuum Aerodynamic Diameters
Source: Informa UK Limited
Influence of Emissions and Aqueous Processing on Particles Containing Black Carbon in a Polluted Urban Environment: Insights From a Soot Particle-Aerosol Mass Spectrometer
Source: American Geophysical Union (AGU)
Laboratory evaluation of species-dependent relative ionization efficiencies in the A
Sour
Influ
es of
aero
Sour
A Ne
t
D
Sou
A me
Sour
The
Sour

In this article

Intercomparison and evaluation of four semi-continuous PM2.5 sulfate instruments

Source: Elsevier BV

Investigation of global particulate nitrate from the AeroCom phase III experiment

Source: Copernicus Publications

Analysis of CCN activity of Arctic aerosol and Canadian biomass burning during summer 2008

Source: Copernicus GmbH

Evaluation of the new capture vaporizer for aerosol mass spectrometers (AMS) through field studies of inorganic species

Source: Taylor & Francis

Investigating the links between ozone and organic aerosol chemistry in a biomass burning plume from a prescribed fire in California chaparral

Source: European Geosciences Union

An Aerosol Chemical Speciation Monitor (ACSM) for Routine Monitoring of the Composition and Mass Concentrations of Ambient Aerosol

Source: Informa UK Limited

High Precision Density Measurements of Single Particles: The Density of Metastable Phases

Source: Informa UK Limited

Impacts of Aerosol Aging on Laser Desorption/Ionization in Single-Particle Mass Spectrometers

Sour

Char ser

Valle

Sour

Deve n

Anal

S

Parti and

Aero

Sour

Ther nass

spec

Numerical Characterization of Particle Beam Collimation: Part II Integrated Aerodynamic-Lens-Nozzle System
Source: Informa UK Limited
Long-term real-time measurements of aerosol particle composition in Beijing, China: seasonal variations, meteorological effects, and source analysis
Source: Copernicus GmbH
Particle Morphology and Density Characterization by Combined Mobility and Aerodynamic Diameter Measurements. Part 1: Theory
Source: Informa UK Limited
ACTRIS ACSM intercomparison - Part 2: Intercomparison of ME-2 organic source apportionment results from 15 individual, co-located aerosol mass spectrometers
Source: HAL CCSD
Aerodynamic Lens System for Producing Particle Beams at Stratospheric Pressures
Source: Informa UK Limited
Thermal plasma deposition of nanophase hard coatings
Source: Elsevier BV
A generalised method for the extraction of chemically resolved mass spectra from aerodyne aerosol mass spectrometer data
Source: Elsevier BV
A differentially pumped particle inlet for sampling of atmospheric aerosols into a time-of-flight mass spectrometer : Optical characterization of the particle beam
Sour
Seco er
Stud
Phot
Sour
G Theory
of Pa
Sour
Colle erated
Seco
Sour

Source: American Geophysical Union (AGU)

Aerosol layers from the 2008 eruptions of Mount Okmok and Mount Kasatochi: In situ upper troposphere and lower stratosphere measurements of sulfate and organics over Europe

Source: American Geophysical Union (AGU)

Measurement of condensed-phase reaction kinetics in the aerosol phase using single particle mass spectrometry

Source: American Chemical Society (ACS)

Real-time chemical analysis of organic aerosols using a Thermal Desorption Particle Beam Mass Spectrometer

Source: Informa UK Limited

A Design Tool for Aerodynamic Lens Systems

Source: Informa UK Limited

Particle mass yield in secondary organic aerosol formed by the dark ozonolysis of α-pinene

Source: Copernicus GmbH

An Eddy-Covariance System for the Measurement of Surface/Atmosphere Exchange Fluxes of Submicron Aerosol Chemical Species—First Application Above an Urban Area

Source: Informa UK Limited

Effect of secondary organic aerosol coating thickness on the real-time detection and characterization of biomass-burning soot by two particle mass spectrometers

Sour

Aero high-

time

Sour

Indo

Sour

I

Sou

Deve

Ther s

Sour

A ma

In this article

Generating Particle Beams of Controlled Dimensions and Divergence: II. Experimental Evaluation of Particle Motion in Aerodynamic Lenses and Nozzle Expansions
Source: Informa UK Limited
Evaluation of Composition-Dependent Collection Efficiencies for the Aerodyne Aerosol Mass Spectrometer using Field Data
Source: Informa UK Limited
Development and characterization of an aerosol time-of-flight mass spectrometer with increased detection efficiency.
Source: American Chemical Society (ACS)
Particle Morphology and Density Characterization by Combined Mobility and Aerodynamic Diameter Measurements. Part 2: Application to Combustion-Generated Soot Aerosols as a Function of Fuel Equivalence Ratio
Source: Informa UK Limited
Size and composition biases on the detection of individual ultrafine particles by aerosol mass spectrometry
Source: American Chemical Society (ACS)
Collection efficiency of α -pinene secondary organic aerosol particles explored via light-scattering single-particle aerosol mass spectrometry
Source: Copernicus GmbH
Design and Operation of a Pressure-Controlled Inlet for Airborne Sampling with an Aerodynamic Aerosol Lens
Source: Informa UK Limited
Char 003
camp -
relat s
Sour

Linki

REFE

1. Alfarra garatna , M. , Jimene

In this article

Using Two Aerodyne Aerosol Mass Spectrometers . Atmos. Environ. , 38 : 5745 – 5758 . [CSA]

Web of Science ® | Google Scholar

2. Allan , J. D. , Bower , K. N. , Coe , H. , Boudries , H. , Jayne , J. T. , Canagaratna , M. R. , Millet , D. B. , Goldstein , A. H. , Quinn , P. K. , Weber , R. J. and Worsnop , D. R. 2004a . Submicron Aerosol Composition at Trinidad Head, California, during ITCT 2K2: Its Relationship With Gas Phase Volatile Organic Carbon and Assessment of Instrument Performance . J. Geophys. Res. Atmos. , 109 (D23524) doi: 10.1029/2003JD004208[CSA]

Google Scholar

3. Allan , J. D. , Delia , A. E. , Coe , H. , Bower , K. N. , Alfarra , M. R. , Jimenez , J. L. , Middlebrook , A. M. , Drewnick , F. , Onasch , T. B. , Canagaratna , M. R. , Jayne , J. T. and Worsnop , D. R. 2004b . A Generalised Method for the Extraction of Chemically Resolved Mass Spectra from Aerodyne Aerosol Mass Spectrometer Data . J. Aerosol Sci. , 35 (7) : 909 – 922 . [CROSSREF] [CSA]

Web of Science ® | Google Scholar

4. Cziczo , P. J. , De Mott , D. J. , Brock , C. , Hudson , P. K. , Jesse , B. , Kreidenweis , S. M. , Prenni , A. J. , Schreiner , J. , Thomson , D. S. and Murphy , D. M. 2003 . A Method for Single Particle Mass Spectrometry of Ice Nuclei . Aerosol Sci. Technol. , 37 (5) : 460 – 470 . [CROSSREF] [CSA]

5. DeCar 2004 . Particl nd Aerod ol. , 38 (12) : 1

6. Delia mposition and In Colorado . Goog

In this article

7. Drewnick , F. , Hings , S. S. , De Carlo , P. , Jayne , J. , Gonin , M. , Fuhrer , K. , Weimer , S. , Jimenez , J. , Demerjian , K. L. , Borrmann , S. and Worsnop , D. 2004 . Application of a Novel Time-of-Flight Aerosol Mass Spectrometer for Chemical Composition Characterization of Urban (New York) aerosol . Aerosol Sci. Technol. , 39 (7) : 637 – 658 . [CROSSREF] [CSA]

Web of Science ® | Google Scholar

8. Drewnick , F. , Schwab , J. J. , Hogrefe , O. , Peters , S. , Husain , L. , Diamond , D. , Weber , R. and Demerjian , K. L. 2003 . Intercomparison and Evaluation of Four Semi-Continuous PM2.5 Sulfate Instruments . Atmos. Environ. , 37 (24) : 3335 – 3350 . [CROSSREF] [CSA]

Web of Science ® | Google Scholar

9. Gard , E. , Mayer , J. E. , Morrical , B. D. , Dienes , T. , Fergenson , D. P. and Prather , K. A. 1997 . Real-Time Analysis of Individual Atmospheric Aerosol Particles: Design and Performance of a Portable ATOFMS . Anal. Chem. , 69 (20) : 4083 – 4091 . [CROSSREF] [CSA]

Web of Science ® | Google Scholar

10. Heberlein , J. , Postel , O. , Girshick , S. , Mc Murry , P. , Gerberich , W. , Iordanoglou , D. , Di Fonzo , F. , Neumann , D. , Gidwani , A. , Fan , M. and Tymiak , N. 2001 . Thermal Plasma Deposition of Nanophase Hard Coatings . Surface & Coatings Technology , 142 : 265 – 271 . [CROSSREF] [CSA]

11. Hogre erjian , K. L. , Rhoac , V. A. 2004 . Semi nd a Rural Loc Air & Waste Ma

12. Jayne lb , C. E. and W r for Size

In this article

and Composition Analysis of Submicron Particles . Aerosol Sci. Technol. , 33 (1–2) : 49 – 70 . [CSA]
Web of Science ® | Google Scholar

13. Jimenez , J. , Seinfeld , J. H. , Flagan , R. C. , Canagaratna , M. , Jayne , J. , Worsnop , D. , Zhang , X. and Smith , K. A. 2001 . " Size Resolution of the Aerodyne Aerosol Mass Spectrometer " . In AAAR Annual Meeting , 2001 Portland : Oregon .
Google Scholar

14. Jimenez , J. L. , Bahreini , R. , Cocker , D. R. , Zhuang , H. , Varutbangkul , V. , Flagan , R. C. , Seinfeld , J. H. , O'Dowd , C. D. and Hoffmann , T. 2003a . New particle Formation from Photooxidation of Diiodomethane (CH2I2) . J. Geophys. Res. Atmos. , 108 (D10) : 4318 doi: 10.1029/2001JD001213[CROSSREF] [CSA]
Web of Science ® | Google Scholar

15. Jimenez , J. L. , Jayne , J. T. , Shi , Q. , Kolb , C. E. , Worsnop , D. R. , Yourshaw , I. , Seinfeld , J. H. , Flagan , R. C. , Zhang , X. F. , Smith , K. A. , Morris , J. W. and Davidovits , P. 2003b . Ambient Aerosol Sampling Using the Aerodyne Aerosol Mass Spectrometer . J. Geophys. Res. Atmos. , 108 (D10) : 4318 doi: 10.1029/2002JD002452[CROSSREF] [CSA]
Web of Science ® | Google Scholar

16. Kane , D. B. and Johnston , M. V. 2000 . Size and Composition Biases on the Detection of Indi ci. Technol. , 34 (2

17. Katrib , D. 2005 . De Atmos. Ch

18. Liu , P erating Particl rticle Motion

In this article

in Aerodynamic Lenses and Nozzle Expansions . Aerosol Sci. Technol. , 22 (3) : 293 – 313 . [CSA]

Web of Science ® | Google Scholar

19. Liu , P. , Ziemann , P. J. , Kittelson , D. B. and Mc Murry , P. H. 1995b . Generating Particle Beams of Controlled Dimensions and Divergence .2. Experimental Evaluation of Particle Motion in Aerodynamic Lenses and Nozzle Expansions . Aerosol Sci. Technol. , 22 (3) : 314 – 324 . [CSA]

Web of Science ® | Google Scholar

20. Mahadevan , R. , Lee , D. , Sakurai , H. and Zachariah , M. R. 2002 . Measurement of Condensed-Phase Reaction Kinetics in the Aerosol Phase Using Single Particle Mass Spectrometry . J. Phys. Chem. A , 106 (46) : 11083 – 11092 . [CROSSREF] [CSA]

Web of Science ® | Google Scholar

21. Middlebrook , A. M. and Matthew , B. 2004 . Personal Communication

Google Scholar

22. Oktem , B. , Tolocka , M. P. and Johnston , M. V. 2004 . On-Line Analysis of Organic Components in Fine and Ultrafine Particles by Photoionization Aerosol Mass Spectrometry . Anal. Chem. , 76 (2) : 253 – 261 . [PUBMED] [INFOTRIEVE] [CROSSREF] [CSA]

PubMed | Web of Science ® | Google Scholar

23. Onasc

Goog

24. Petruc

Dif into a Time-

of- n . Aerosol

Sci. Te

25. Salced Onasch , T.

In this article

Aerosols in Mexico City using an Aerosol Mass Spectrometer . Atmos. Chem. Phys. , 5 : 4143 – 4182 . [CSA]
Google Scholar

26. Schreiner , J. , Schild , U. , Voigt , C. and Mauersberger , K. 1999 . Focusing of Aerosols into a Particle Beam at Pressures from 10 to 150 Torr . Aerosol Sci. Technol. , 31 (5) : 373 – 382 . [CROSSREF] [CSA]
Web of Science ® | Google Scholar

27. Schreiner , J. , Voigt , C. , Mauersberger , K. , McMurry , P. and Ziemann , P. 1998 . Aerodynamic Lens System for Producing Particle Beams at Stratospheric Pressures . Aerosol Sci. Technol. , 29 (1) : 50 – 56 . [CSA]
Web of Science ® | Google Scholar

28. Schreiner , J. , Voigt , C. , Zink , P. , Kohlmann , A. , Knopf , D. , Weisser , P. , Budz , C. and Mauersberger , K. 2002 . A Mass Spectrometer System for Analysis of Polar Stratospheric Aerosols . Review of Scientific Instruments , 73 (2) : 446 – 452 . [CROSSREF] [CSA]
Web of Science ® | Google Scholar

29. Serway , R. A. 1996 . Physics For Scientists and Engineers , 696 Saunders College Publishing .
Google Scholar

30. Slowik olb , C. E. , Worsn phology and Densit er Measu es as a Fur 5 – 1222 . [CR

31. Su , Y. nt and Chara reased

In this article

Detection Efficiency . Anal. Chem. , 76 (3) : 712 – 719 . [PUBMED] [INFOTRIEVE] [CROSSREF] [CSA]

PubMed | Web of Science ® | Google Scholar

32. Svane , M. , Hagstrom , M. and Pettersson , J. B. C. 2004 . Chemical Analysis of Individual Alkali-Containing Aerosol Particles: Design and Performance of a Surface Ionization Particle Beam Mass Spectrometer . Aerosol Sci. Technol. , 38 (7) : 655 – 663 . [CROSSREF] [CSA]

Web of Science ® | Google Scholar

33. Sykes , D. C. , Woods , E. , Smith , G. D. , Baer , T. and Miller , R. E. 2002 . Thermal Vaporization-Vacuum Ultraviolet Laser Ionization Time-of-Flight Mass Spectrometry of Single Aerosol Particles . Anal. Chem. , 74 (9) : 2048 – 2052 . [PUBMED] [INFOTRIEVE] [CROSSREF] [CSA]

PubMed | Web of Science ® | Google Scholar

34. Tafreshi , H. V. , Benedek , G. , Piseri , P. , Vinati , S. , Barborini , E. and Milani , P. 2002 . A Simple Nozzle Configuration for the Production of Low Divergence Supersonic Cluster Beam by Aerodynamic Focusing . Aerosol Sci. Technol. , 36 (5) : 593 – 606 . [CROSSREF] [CSA]

Web of Science ® | Google Scholar

35. Tobias , H. J. , Kooiman , P. M. , Docherty , K. S. and Ziemann , P. J. 2000 . Real-Time Chem e Beam Mass

36. Weime rsini , D. A. , Ca ve Non- Re Winter Intens Goog

37. Zelen light Mass

In this article

[CSA]

Web of Science ® | Google Scholar

38. Zelenyuk , A. , Cabalo , J. , Baer , T. and Miller , R. E. 1999 . Mass Spectrometry of Liquid Aniline Aerosol Particles by IR/UV Laser Irradiation . Anal. Chem. , 71 (9) : 1802 – 1808 . [CROSSREF] [CSA]

PubMed | Web of Science ® | Google Scholar

39. Zhang , Q. , Canagaratna , M. , Jayne , J. , Worsnop , D. and Jimenez , J. 2004a . Time and Size-Resolved Chemical Composition of Submicron Particles in Pittsburgh-Implications for Aerosol Sources and Processes . J. Geophys. Res.—Atmos. , 110 (D7) : D07S09 doi: 10.1029/2004JD004649[CROSSREF] [CSA]

Web of Science ® | Google Scholar

40. Zhang , Q. , Stanier , C. O. , Canagaratna , M. , Jayne , J. , Worsnop , D. , Pandis , S. N. and Jimenez , J. 2004b . Insights into the Chemistry of Nucleation Bursts and New Particle Growth Events in Pittsburgh Based on Aerosol Mass Spectrometry . Environ. Sci. Technol. , 38 : 4797 – 4809 . [PUBMED] [INFOTRIEVE] [CROSSREF] [CSA]

PubMed | Web of Science ® | Google Scholar

41. Zhang , X. F. , Smith , K. A. , Worsnop , D. R. , Jimenez , J. , Jayne , J. T. and Kolb , C. E. 2002 . A Numerical Characterization of Particle Beam Collimation by an Aerodynamic Lens-Nozzle System: Part I. An Individual Lens or Nozzle . Aerosol Sci. Technol. , 36 (5) : 617

42. Zhang Kolb , C. E. , Morris e Beam Col Sci. Tec

43. Zhang

Goog

In this article

Download PDF

Related research

People also read | Recommended articles | Cited by 151

Information for

- Authors
- R&D professionals
- Editors
- Librarians
- Societies

Open access

- Overview
- Open journals
- Open Select
- Dove Medical Press
- F1000Research

Opportunities

- Reprints and e-prints
- Advertising solutions
- Accelerated publication
- Corporate access solutions

Help and information

- Help and contact
- Newsroom
- All journals
- Books

Keep up to date

Register to receive personalised research and resources by email

Sign

In this article